A High-Resolution High-Sensitivity Standoff Imaging System at 350 GHz

Daniel Becker*†, Cale Gentry‡, James Beall*, Hsiao-Mei Cho*, William Duncan*, Gene Hilton*, Kent Irwin*, Peter Lowell*, Michael Niemack*, Nick Paulter*, Carl Reintsema*, Frank Schima*, Robert Schwall*, Peter Ade§, Carole Tucker§, Simon Dicker¶, Mark Halpern‖
*National Institute of Standards and Technology
Boulder, Colorado 80303
Email: beckerd@boulder.nist.gov
†University of Colorado
‡University of Oklahoma
§Cardiff University
¶University of Pennsylvania
‖University of British Columbia

***Abstract*—Millimeter-wavelength radiation holds promise for detection of security threats at a distance, including suicide bomb belts and maritime threats in poor weather conditions. The sensitivity provided by superconducting Transition-Edge-Sensor (TES) bolometers makes them ideal for high-sensitivity passive imaging of thermal signals at millimeter and sub-millimeter wavelengths. We are developing a 350 GHz video-rate imaging system using 800 TES bolometers as detectors. This demonstration system takes images at distances from 16 m to 28 m. When operating at 16 m, the resolution is 1 cm over a 1 m × 1 m field of view. The system is predicted to take video images with a noise-equivalent temperature difference of 200 mK at 20 frames per second. Light is captured by an f/2.0 Cassegrain optical system with 1.3 m primary mirror. The detectors are read out using a time-domain multiplexed SQUID readout system. We report on the current status of development of this system.**

I. INTRODUCTION

Millimeter-wavelength radiation penetrates clothing and is non-ionizing, making it a good candidate for identifying threats held beneath clothing [1]. Portal millimeter-wave systems are commercially available and have been deployed at airports and other sites around the world. These systems produce low-noise images but require the person being scanned to stand still within a booth.

To safely detect threats such as suicide bomb belts, images must be taken while the person being scanned is farther away. These "stand-off" imaging systems face challenges that portal systems do not, including an uncontrolled environment, moving subjects (requiring video-rate imaging), increased atmospheric attenuation and an increase in required angular resolution.

Millimeter-wave stand-off imaging systems fall into two categories: active and passive. Active imaging systems illuminate the observation target with millimeter-wave light and form images by interpreting the light that is reflected back. Active systems offer excellent noise performance but face several challenges, including specular reflections and scaling to large numbers of detectors. The recent development of millimeter-wave radar systems is promising in this area [2]. Passive imaging systems detect thermal emissions, with contrast provided by low-emissivity concealed objects reflecting light that is colder than body temperature. Passive video imaging systems are available commercially [3], but have poor spatial and temperature resolution at frame rates faster than 5 frames per second. Cryogenic passive imaging systems using superconducting transition edge sensors are also being developed. One system with 64 detectors produces video images with a noise equivalent temperature difference (NETD) of 0.5 K at 6 frames per second with a resolution of 4 cm over a 2 m × 4 m area [4]–[7]. Another system has much lower noise on a per-detector basis, but currently has only 10 detectors [8].

We are developing a cryogenic passive video imaging system for operation at distances from 16 m to 28 m. The system will contain 800 photon-noise-limited TES bolometers read out by superconducting quantum interference devices (SQUIDs) using a multiplexer developed at NIST. The system will be used as a test-bed to explore trade-offs between NETD, resolution and video frame rate, with the goal of understanding performance requirements for specific real-world stand-off imaging applications.

The system will operate at a frequency of 350 GHz (850 μm) with 11 % fractional bandwidth. Spatial resolution will be 1 cm over a 1 m × 1 m field of view at a distance of 16 m, with a video rate of 20 frames per second. Measurements of prototype detectors and the system's optical efficiency indicate that the fully populated focal plane with 800 detectors should achieve NETD of 200 mK at 20 frames per second. This paper describes the optics, detectors, readout, cryogenics and current status of this system.

II. DESIGN OVERVIEW

A. Optical Frequency Choice

The choice of frequency for a passive imaging system is a tradeoff between the ability to penetrate clothing (favoring low frequencies) and spatial resolution (favoring high frequencies).

US government contribution; not subject to copyright in the United States.

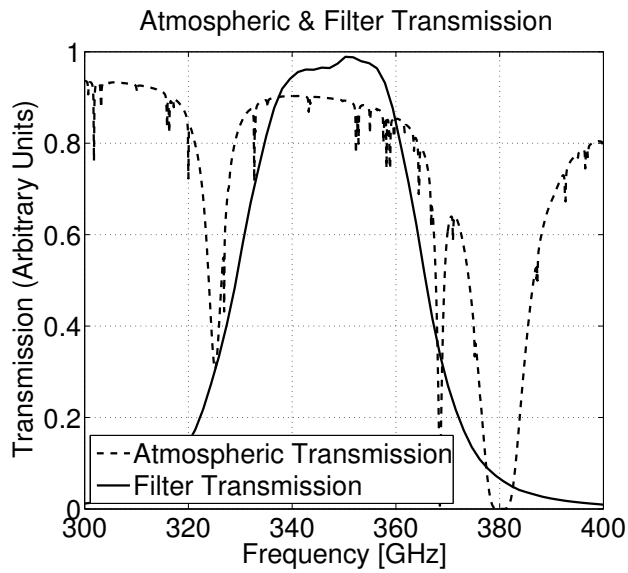

Fig. 1. Plot showing measured transmission of our bandpass filter (solid lines) and typical atmospheric transmission (dashed lines). The passband is centered at approximately 350 GHz (850 μm) and has a full width at half-maximum of about 11 %.

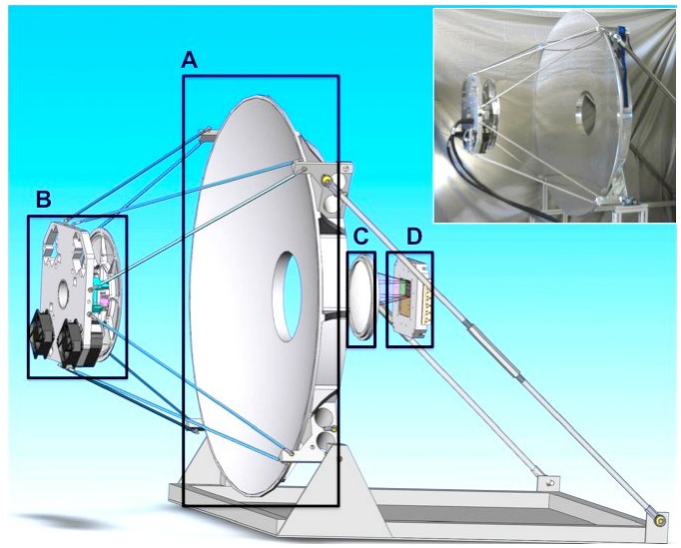

Fig. 2. Schematic of optical system. Labels are (A) 1.3 m primary mirror, (B) secondary mirror with dithering mechanism, (C) cryostat window lens, (D) detector focal plane module, including bandpass filter. For clarity, the cryostat is not shown. Inset is a photograph of the primary and secondary mirror assembly.

The 3 dB point for attenuation through clothing ranges from 350 GHz to 1 THz (high frequencies for thin materials such as Nylon, lower for thicker materials such as wool) [9]. We chose 350 GHz to keep clothing attenuation at or below 3 dB and provide good spatial resolution. This frequency is also the center of an atmospheric transmission band (see Fig. 1).

B. Optics

Our optical system is an f/2.0 Cassegrain design. The 1.3 m elliptical primary mirror focuses light onto the hyperbolic secondary, which directs the light back through the central hole in the primary; the light then enters an ultra-high-molecular-weight (UHMW) polyethylene lens at the mouth of the cryostat. The lens makes the system telecentric, allowing use of a flat focal plane. The lens/cryostat combination can be moved relative to the primary mirror to focus the system at distances between 16 m and 28 m. The optics were simulated with ray-tracing software and shown to be diffraction-limited across the entire focal plane and at all focusing distances between 16 m and 28 m. See Fig. 2 for an annotated picture of the optical system. A detailed description of the optics has been published elsewhere [10], [11].

The observation band is defined by a metal mesh filter [12] cooled to 900 mK, defining an optical bandwidth of 40 GHz (11 % FWHM fractional bandwidth); the measured passband of this filter is shown in Fig. 1. Additional filters for thermal blocking are located at the 4 K, 50 K, and 300 K stages [13]. Total transmittance of the filter stack plus lens is predicted to be 62 %.

At the focal plane, light is captured by smooth-walled conical feedhorns that were chosen for their simplicity and ease of manufacture. To optimize coupling of the feedhorns to the rest of the optical system, we use feedhorns with a diameter of 3.2 mm, or approximately $2F\lambda$, where $F = 2.0$ is the f-number of the optics and $\lambda = 850$ μm is the optical wavelength. The taper half-angle is 9.4°, tapering to a 3.5 mm length of 0.6 mm diameter circular waveguide that leads to the detectors. Finite-element electromagnetic simulations predict that the feedhorns will have a spillover efficiency of 54 %. Conductive loss in the 3.5 mm length of 0.6 mm waveguide behind the feedhorn is calculated to be about 10 %.

At the back of the 0.6 mm circular waveguide, in front of a quarter-wave backshort, the light is absorbed by a PdAu mesh patterned on a relieved membrane as described in section II-D. Finite-element electromagnetic models predict that the PdAu mesh will absorb 82 % of the optical power coming down the waveguide. The mesh absorbs both polarizations.

Because the point-spread-function of the optics has size $F\lambda$ on the focal plane, the feedhorns will be spaced farther apart than the Nyquist limit. Additionally, the feedhorns will cover only a portion of the diffraction-limited area of the focal plane. To generate fully sampled images, and to use the entire diffraction-limited extent of the optics, the secondary mirror will be moved by a set of actuators. This "dithering" of the secondary mirror will move the image across the focal plane, allowing fully sampled video images to be generated across the entire 1 m^2 target area.

C. Transition Edge Sensors

Optical power is detected by voltage-biased superconducting transition edge sensor (TES) bolometers [14], [15]. Below a critical temperature, T_c, a superconductor loses all resistance to DC electrical current (see Fig. 3). The sharp transition from the normal state to superconducting state allows a superconductor that has been biased into its transition to serve as a sensitive thermometer. Any signal that can be turned into a temperature

change can then be detected as a change in the resistance of the superconductor. Reference [16] contains a detailed description of the behavior of TES devices.

Fig. 4 schematically depicts the operation of a voltage-biased TES bolometer. A superconducting film is thermally sunk to an optical absorber. An increase in incoming optical power raises the temperature of the film, increasing the resistance of the TES, which decreases the current passing through the circuit. A SQUID detects the drop in current. The device operates in a negative-feedback loop, with increasing optical power leading to lower V^2/R Joule heating, allowing the device to operate stably.

A weak thermal link connects the absorber and superconducting film to a low-temperature heat bath. The thermal conductance of this link determines the saturation power P_{sat} according to $P_{sat} = K(T_c^n - T_{bath}^n)$, where K and n depend on the geometry of the thermal link and the dominant heat transport mechanism in the temperature regime of interest; for our detectors we expect $n \approx 4.0$.

The dominant source of intrinsic noise in a TES bolometer is thermal fluctuations of the temperature of the TES itself. This noise is $NEP_G = F\sqrt{4k_B G T_c^2}$, where k_B is Boltzmann's constant and the differential thermal conductance G is defined as $G = dP/dT_c = nKT_c^{n-1}$. The prefactor F is unity in equilibrium, and in the range 0.5–1.0 under operating conditions.

Photon noise is also a significant source of noise in our system. The expression for photon noise, including the effect of photon bunching, is [17]

$$NEP_{ph} = \sqrt{2h\nu P_{opt}(1 + \eta\bar{n})}, \tag{1}$$

where h is Planck's constant, ν is the central frequency, P_{opt} is the total optical loading, η is the optical efficiency (excluding feedhorn spillover efficiency, because the feedhorn spillover is terminated at 300 K), and $\bar{n} = [exp(h\nu/k_B T) - 1]^{-1}$ is the average photon occupation number per mode. For our system observing 300 K radiation, $\bar{n} = 17.5$, so the bunching term is important. Total optical power per detector when observing a 300 K target will be $2\eta k_B T \Delta\nu = 165$ pW. Use of (1) then gives $NEP_{ph} = 0.8$ fW/$\sqrt{\text{Hz}}$.

D. Design of Prototype Detectors

Fig. 5 shows a picture of one of our prototype detectors. The device is fabricated on a relieved silicon-nitride membrane approximately 800 μm in diameter. A PdAu mesh absorbs the light, with mesh dimensions (2 μm wide lines spaced 85 μm apart) chosen to match the wave impedance of the waveguide. The Al TES is at the lower edge of the membrane and has dimensions 64 μm $\times$ 64 μm. A 15 μm $\times$ 16 μm PdAu heater resistor sits near the center of the relieved membrane for use in testing.

We designed our detectors to have $P_{sat} = 1$ nW at a bath temperature of 900 mK, for a safety factor of 6 times the predicted optical loading of 165 pW. Given this saturation power, an Al TES with $T_c = 1.2$ K, a bath at 900 mK, and a target G of 4.5 nW/K should meet our NETD requirements.

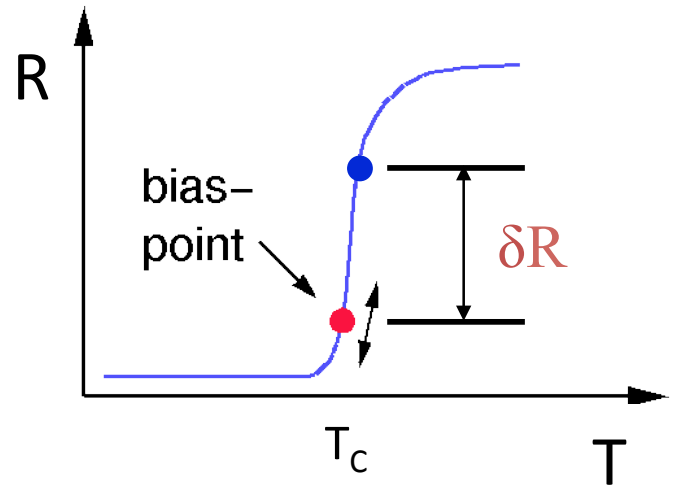

Fig. 3. Illustrative plot of resistance vs temperature for a superconductor. The transition is typically very narrow, allowing the use of a superconductor as a sensitive thermometer. A TES detector is voltage-biased into the transition, with the bias point changing based on changes in optical power.

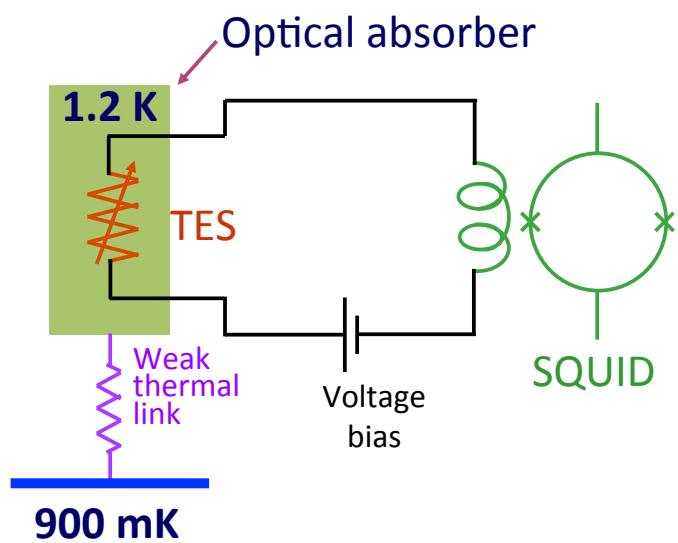

Fig. 4. Schematic depiction of the operation of a TES. Optical power is absorbed onto the TES. Increases in absorbed optical power raises the temperature of the TES, raising its resistance. The dissipated V^2/R Joule power in the TES drops, compensating for the increase in optical power, leaving as constant the total dissipated power flowing out of the TES through the weak thermal link. This negative electro-thermal feedback allows the detector to operate stably. Changes in current passing through the TES are detected by a SQUID.

The dimensions of the eight silicon-nitride legs (11 μm wide $\times$ 40 μm long, 0.5 μm thick) were chosen to achieve this G.

This large thermal conductance requires a large heat capacity C to keep the thermal time constant near the 1 ms that is optimal for our readout system. We have achieved this by adding a 2 μm thick gold ring around the outer diameter of the relieved membrane.

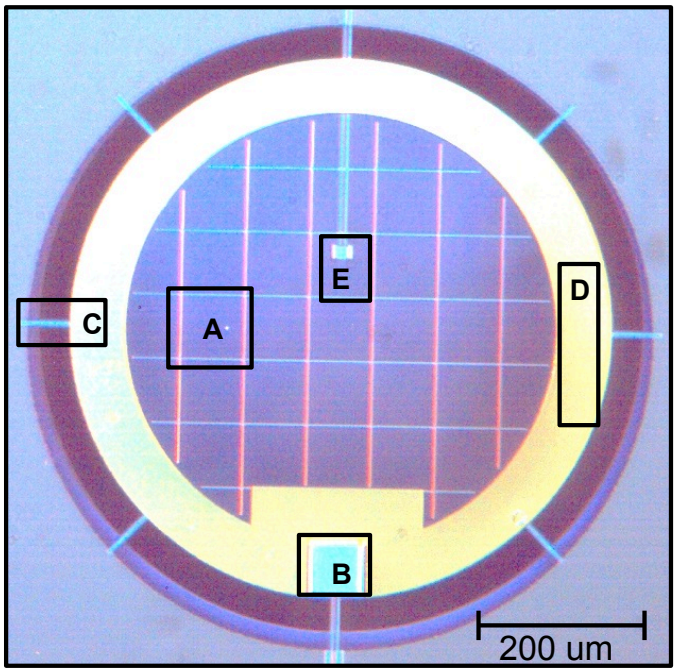

Fig. 5. A picture of one of our prototype TES detectors. The relieved area is 800 μm in diameter. The different components are: (A) PdAu absorbing mesh, lines 2 μm wide spaced 85 μm apart, (B) thin-film Al TES, (C) silicon-nitride legs connecting relieved membrane to the bulk Si substrate that serves as low-temperature bath, (D) Au ring providing additional heat capacity to slow the thermal response time of the device for optimal readout, (E) PdAu heater resistor used for testing.

E. Readout

The array is read out by the SQUID-based time-division multiplexing (TDM) system developed at NIST [18]. At room temperature a single Multi-Channel Electronics (MCE) crate will read out all 800 detectors [19]. The combination of NIST SQUID TDM with the MCE is used daily to collect data at three different millimeter-wave telescopes; see [20]–[22]. All hardware for the full 800 detector array, including cryogenic wiring, is already installed in our cryostat.

F. Cryogenics

To cool our focal plane to an operating bath temperature of 900 mK, we use a two-stage refrigeration system. The first stage is a commercially available cryogen-free Gifford-McMahon cryocooler that reaches 3 K. The second stage is a custom-built ^{4}He sorption fridge that cools to below 1 K, and is based on a design that has been proven in the field [23]. The system reaches a base temperature of approximately 900 mK with a hold time of 13.5 hours when open optically. Operation of the cryogenics will be fully automated.

III. CURRENT STATUS

We have installed four prototype detectors into our cryostat. Individual modules with feedhorns integrated into their cover hold each detector. All data discussed in this section were taken with the complete multiplexed readout chain configured in a 2 row $\times$ 2 column format.

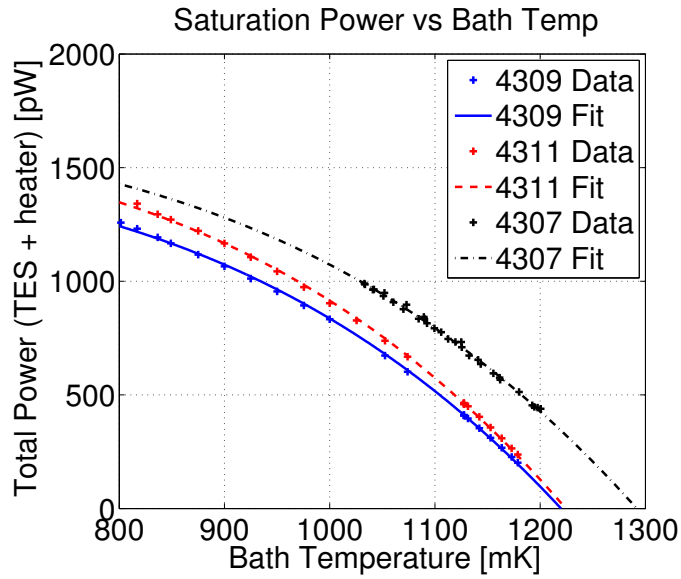

Fig. 6. Plot showing saturation power P_{sat} vs bath temperature for three of our prototype devices. Fitting all three parameters n, K, and T_c implies $n \approx 3.6$. The fit constrains n weakly, so for this paper we assume $n = 4.0$ everywhere; this increases our predicted detector noise by a few percent. Detector 4307 was measured in a different cryostat with different thermometry, which could explain the temperature offset from detectors 4309 and 4311.

A. Dark Testing

The prototype devices have a transition temperature of approximately 1.23 K, with a normal-state resistance of about 3.5 mΩ. Fig. 6 shows measured saturation power vs. bath temperature for three tested devices; the measured G values are 5.0 nW/K to 5.4 nW/K. These values of G imply NEP_G of 0.64 fW/$\sqrt{\text{Hz}}$ to 0.69 fW/$\sqrt{\text{Hz}}$, assuming a prefactor F of 1.0. The measured NEP for one of our detectors is shown in Fig. 7. The measured noise level matches the prediction well.

Adding the detector and expected photon noise in quadrature gives $NEP_{tot} = 1.1$ fW/$\sqrt{\text{Hz}}$. This total NEP can be converted to an NETD through the use of the radiometer equation [24],

$$NETD = \frac{NEP_{tot}}{2k_B \Delta\nu\eta\sqrt{2\tau}}, \tag{2}$$

where τ is the total integration time per pixel in the processed video frame, $\Delta\nu = 40$ GHz is the pre-detection optical bandwidth, and $\eta = 0.25$ is the total optical efficiency (0.82 absorber efficiency, 0.62 filter stack efficiency, 0.54 feedhorn spillover efficiency and 0.90 feedhorn insertion loss). Creating a 1 m^2 image with 1 cm resolution requires 200^2 pixels per video frame. With an 800 detector system, this leads to a "dithering factor" of $200^2/800 = 50$, meaning that each detector will image 50 image pixels per video frame, and $\tau = 1/(50)(20\text{ Hz})$. Equation 2 thus predicts that our system will have $NETD = 85$ mK across the full field of view at 20 FPS.

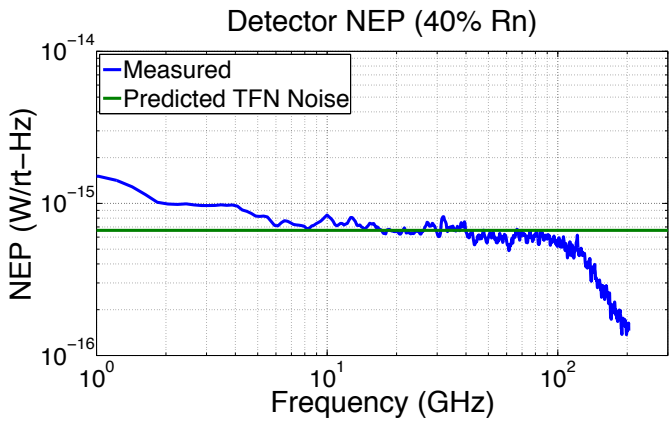

Fig. 7. Plot showing measured noise equivalent power (NEP) spectral density for one of our detectors. The white noise level is about 0.65 fW/$\sqrt{\text{Hz}}$. The low-frequency increase in noise is due to a drift in bath temperature that we are fixing. The 120 Hz rolloff is due to a filter in the readout electronics that was turned on while acquiring this spectrum.

B. Optical Testing

Our optical testing has focused on two areas: measuring optical efficiency and taking still images.

To measure total optical efficiency we measure the difference in detected optical power between when the imager is observing 295 K and 77 K blackbodies in the 16 m distant focal plane. The ratio of this difference in optical power to $2k_B\Delta T\Delta\nu$ is the total optical efficiency of the system. The 295 K blackbody is a sheet of room-temperature Eccosorb AN-72 attached to an aluminum backing sheet. The 77 K blackbody is a sheet of Eccosorb AN-72 submerged in liquid nitrogen held in a styrofoam cooler with walls approximately 2.5 cm thick. We apply a correction to account for the imperfect transmission of the styrofoam cooler's walls, which we measured by moving the cooler's lid back and forth in front of the cooler. This measurement approach resulted in an average optical efficiency of 11.5 % for the four detectors, about half of the predicted value of 26 %. We have not yet identified the source of the lost efficiency, but it is likely that some of the loss is due to poor alignment of the cryostat with the primary and secondary mirrors.

We do not yet have enough detectors installed to take video images. But we can take still images by using the secondary mirror to raster scan over the target. Fig. 8 shows an image of a person with a ceramic knife concealed beneath his shirt. This image includes data from three detectors, with a large area of overlap near the image center. The knife is visible on the left side. Also visible is the outline of a pocket, the shirt collar, and the line of extra cloth backing the shirt's buttons.

To produce this image, we combined data simultaneously acquired by three detectors. First, data from each detector were used to create three sub-images. Each subimage was then deconvolved by use of the measured point-spread-function of the system, which has the effect of both (a) reducing noise on spatial scales smaller than the system's resolution, and (b) improving apparent resolution. An edge taper was then applied to each sub-image, and finally all three sub-images were combined.

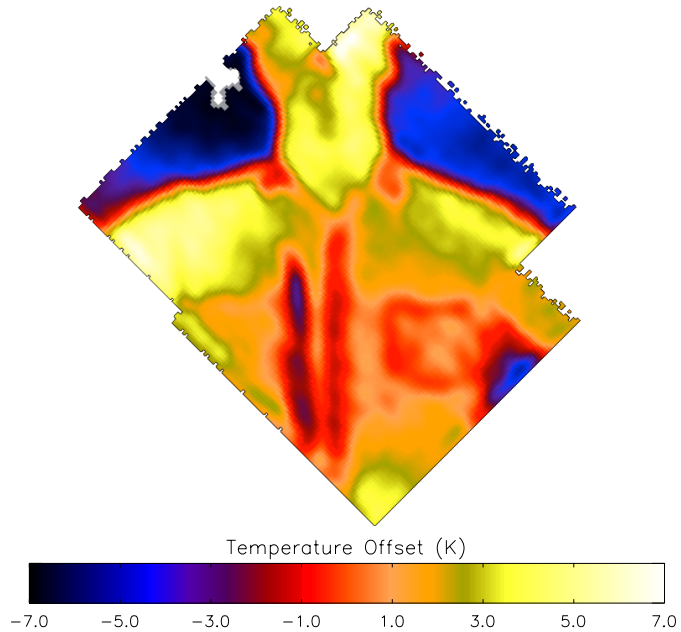

Fig. 8. A sample still image taken with our system. The image was taken by raster scanning across a person with a ceramic knife concealed beneath his shirt. The image NETD is 85 mK, with a total image contrast of 14 K. The contrast between the knife and the warm part of the body next to it is 3.9 K. The total time to acquire the image was 50 s, with an average of 5.5 ms integration time per image pixel.

The temperature scale was calibrated by use of the heaters and the measured optical efficiency. The expected contrast in the image is 12 K (skin temperature of 310 K with emissivity of 0.80, lab background temperature of 295 K). The total contrast in the image is 14 K, indicating that the calibration is reasonable. We estimate the image NETD by taking the standard deviation of pixel temperature values in a flat area of the image. This yields an image NETD of 85 mK, which is about what we expect given the integration time per image pixel of 5.5 ms and the measured optical efficiency. The integration time per image pixel for video images will be 1 ms, so the implied NETD for video rate images is 85 mK $\times\sqrt{5.5} = 200$ mK. This is approximately two times higher than predicted in section III-A. The poor measured optical efficiency explains this discrepancy.

IV. NEXT-GENERATION SYSTEM

The current system features high sensitivity and low noise to facilitate the investigation of the tradeoffs inherent in an operational system. Adapting this system for field deployment will require reduction in cost, weight, and complexity. In addition to modifications such as molded composite optical elements and simplified cryogenics, we are planning to read out a next-generation system with gigahertz micro-resonators that can read out focal planes of either TESs or Microwave Kinetic Inductance Devices (MKIDs) [25]. This technology can read out hundreds of detectors with a single coaxial cable,

greatly reducing the cost and complexity of cryogenic wiring, and allowing focal planes with larger numbers of detectors.

V. CONCLUSION

We have designed a 350 GHz cryogenic terrestrial passive video imaging system by leveraging technology proven in the millimeter and sub-millimeter astronomy field. The video imager will use 800 TES bolometers to image a 1 m $\times$ 1 m field to a resolution of 1 cm at a distance of 16 m at video frame rates. Measurements of our prototype detectors indicate that they are close to being photon-noise-limited. Initial optical testing indicates that the fully populated system will take video-rate images with 200 mK NETD. Improving NETD to the predicted 85 mK requires improving our poor optical efficiency, but requires no changes to the detector design. Our next steps are to design, fabricate, and install the full 800-detector focal plane.

REFERENCES

[1] R. Appleby, "Passive millimetre–wave imaging and how it differs from terahertz imaging," *Philosophical Transactions A*, vol. 362, no. 1815, p. 379, 2004.

[2] K. Cooper, R. Dengler, N. Llombart, T. Bryllert, G. Chattopadhyay, E. Schlecht, J. Gill, C. Lee, A. Skalare, I. Mehdi *et al.*, "Penetrating 3-D imaging at 4-and 25-m range using a submillimeter-wave radar," *Microwave Theory and Techniques, IEEE Transactions on*, vol. 56, no. 12, pp. 2771–2778, 2008.

[3] C. Mann, "First demonstration of a vehicle mounted 250GHz real time passive imager," in *Proceedings of SPIE*, vol. 7311, 2009, p. 73110Q.

[4] A. Luukanen and J. Pekola, "A superconducting antenna-coupled hot-spot microbolometer," *Applied Physics Letters*, vol. 82, p. 3970, 2003.

[5] E. Grossman, C. Dietlein, J. Bjarnason, A. Luukanen, M. Leivo, and J. Pentilla, "THz microbolometers for imaging applications," in *Infrared, Millimeter and Terahertz Waves, 2008. IRMMW-THz 2008. 33rd International Conference on*, 2008, pp. 1–1.

[6] A. Luukanen, P. Helistö, P. Lappalainen, M. Leivo, A. Rautiainen, H. Toivanen, H. Seppä, Z. Taylor, C. Dietlein, and E. Grossman, "Stand-off passive THz imaging at 8-meter stand-off distance: results from a 64-channel real-time imager," in *Proceedings of SPIE*, vol. 7309, 2009, p. 73090F.

[7] A. R. Luukanen, L. Grnberg, M. Grnholm, P. Lappalainen, M. Leivo, E. N. Grossman, and C. R. Dietlein, "Real-time passive terahertz imaging system for standoff concealed weapons imaging," in *Proceedings of SPIE*, vol. 7670, 2010, pp. 7670–3.

[8] E. Heinz, D. Born, G. Zieger, T. May, T. Krause, A. Krüger, M. Schulz, S. Anders, V. Zakosarenko, H. Meyer *et al.*, "Progress report on Safe VISITOR: approaching a practical instrument for terahertz security screening," in *Proceedings of SPIE*, vol. 7670, 2010, p. 767005.

[9] J. Bjarnason, T. Chan, A. Lee, M. Celis, and E. Brown, "Millimeter-wave, terahertz, and mid-infrared transmission through common clothing," *Applied Physics Letters*, vol. 85, no. 4, pp. 519–521, 2004.

[10] W. Duncan, R. Schwall, K. Irwin, J. Beall, C. Reintsema, W. Doriese, H. Cho, B. Estey, G. Chattopadhyay, P. Ade *et al.*, "An Optical System for Body Imaging from a Distance Using Near-TeraHertz Frequencies," *Journal of Low Temperature Physics*, vol. 151, no. 3, pp. 777–783, 2008.

[11] D. Becker, J. Beall, H. Cho, W. Duncan, G. Hilton, R. Horansky, K. Irwin, P. Lowell, M. Niemack, N. Paulter *et al.*, "A 350-GHz high-resolution high-sensitivity passive video imaging system," in *Proceedings of SPIE*, vol. 7670, 2010, p. 76700M.

[12] P. Ade, G. Pisano, C. Tucker, and S. Weaver, "A review of metal mesh filters," in *Proceedings of SPIE*, vol. 6275, 2006, pp. 62 750U–1.

[13] C. Tucker and P. Ade, "Thermal filtering for large aperture cryogenic detector arrays," in *Proceedings of SPIE*, vol. 6275, 2006, p. 62750T.

[14] K. Irwin, "An application of electrothermal feedback for high resolution cryogenic particle detection," *Applied Physics Letters*, vol. 66, p. 1998, 1995.

[15] A. Lee, P. Richards, S. Nam, B. Cabrera, and K. Irwin, "A superconducting bolometer with strong electrothermal feedback," *Applied Physics Letters*, vol. 69, p. 1801, 1996.

[16] K. D. Irwin and G. C. Hilton, *Cryogenic Particle Detection*. Springer-Verlag Berlin Heidelberg, 2005, ch. Transition Edge Sensors, pp. 63–149.

[17] J. Zmuidzinas, "Thermal noise and correlations in photon detection," *Applied optics*, vol. 42, no. 25, pp. 4989–5008, 2003.

[18] P. de Korte, J. Beyer, S. Deiker, G. Hilton, K. Irwin, M. MacIntosh, S. Nam, C. Reintsema, L. Vale, and M. Huber, "Time-division superconducting quantum interference device multiplexer for transition-edge sensors," *Review of Scientific Instruments*, vol. 74, p. 3807, 2003.

[19] E. Battistelli, M. Amiri, B. Burger, M. Halpern, S. Knotek, M. Ellis, X. Gao, D. Kelly, M. Macintosh, K. Irwin *et al.*, "Functional description of read-out electronics for time-domain multiplexed bolometers for millimeter and sub-millimeter astronomy," *Journal of Low Temperature Physics*, vol. 151, no. 3, pp. 908–914, 2008.

[20] D. Swetz, P. Ade, C. Allen, M. Amiri, J. Appel, E. Battistelli, B. Burger, J. Chervenak, A. Dahlen, S. Das *et al.*, "Instrument design and characterization of the millimeter Bolometer Array Camera on the Atacama Cosmology Telescope," in *Proceedings of SPIE*, vol. 7020, 2008, p. 702008.

[21] W. Holland, W. Duncan, B. Kelly, K. Irwin, A. Walton, P. Ade, and E. Robson, "SCUBA-2: a large-format submillimeter camera on the James Clerk Maxwell Telescope," in *Proceedings of SPIE*, vol. 4855, 2003, p. 1.

[22] R. Ogburn IV, P. Ade, R. Aikin, M. Amiri, S. Benton, J. Bock, J. Bonetti, J. Brevik, B. Burger, C. Dowell *et al.*, "The BICEP2 CMB polarization experiment," in *Proceedings of SPIE*, vol. 7741, 2010, p. 77411G.

[23] M. Devlin, S. Dicker, J. Klein, and M. Supanich, "A high capacity completely closed-cycle 250 mK 3He refrigeration system based on a pulse tube cooler," *Cryogenics*, vol. 44, no. 9, pp. 611–616, 2004.

[24] R. Dicke, "The measurement of thermal radiation at microwave frequencies," *Review of Scientific Instruments*, vol. 17, no. 7, pp. 268–275, 1946.

[25] B. Mazin, P. Day, K. Irwin, C. Reintsema, and J. Zmuidzinas, "Digital readouts for large microwave low-temperature detector arrays," *Nuclear Instruments and Methods in Physics Research Section A: Accelerators, Spectrometers, Detectors and Associated Equipment*, vol. 559, no. 2, pp. 799–801, 2006.